processes

MDPI

Article

Experimental Study on Edge Water Invasion of Strongly Heterogeneous Carbonate Gas Reservoirs Based on NMR Technology

Jiangtao Hu [1], Shenglai Yang [1,*], Yi Jiang [1,2], Hui Deng [2,3], Mengyu Wang [2], Li You [1], Qinyi Li [1], Haoyan Bai [1] and Bin Shen [1,*]

[1] National Key Laboratory of Petroleum Resources and Engineering, China University of Petroleum (Beijing), Beijing 102249, China
[2] Exploration and Development Research Institute, PetroChina Southwest Oil & Gasfield Company, Chengdu 610041, China
[3] Sichuan Petroleum Administration Co., Ltd., Chengdu 610051, China
* Correspondence: yangsl@cup.edu.cn (S.Y.); binshen0803@163.com (B.S.)

Abstract: Controlling the extent of water invasion in the reservoir and mitigating its detrimental effects on gas well production and natural gas recovery have long been a challenging task in the efficient development of strongly heterogeneous edge water gas reservoirs. To elucidate the edge water invasion mechanism of strongly heterogeneous carbonate gas reservoirs, this study investigates the pore throat characteristics and fluid mobility from both qualitative and quantitative aspects, leveraging natural core observations, cast thin sections, scanning electron microscopy (SEM), and nuclear magnetic resonance (NMR) tests with centrifuge experiments. A core-scale edge water invasion simulation experiment was conducted under online NMR monitoring to examine the dynamic gas production characteristics of the three types of reservoirs during the water invasion process and to elucidate the formation mechanism and distribution pattern of water-sealed gas. Research findings indicate that carbonate reservoirs typically exhibit a diverse range of pore types, including various types of fractures and cavities. Fractures significantly enhance reservoir connectivity, thereby increasing fluid mobility, but also lead to strong non-uniform water invasion. In contrast, cavities substantially improve the storage capacity of the reservoir and can retard the advancement of the water invasion front, thereby alleviating the adverse effects of water invasion. The ultimate recovery rates of fracture-type, cavity-type, and fracture-cavity cores in the water invasion simulation experiment were 29.81%, 64.87%, and 53.03%, respectively. Premature water breakthroughs in the reservoir can result in a large number of gases in matrix pores and even cavities being sealed by formation water, rendering them unrecoverable, which seriously impacts the gas recovery rate of the reservoir.

Keywords: strongly heterogeneous carbonate; water invasion; NMR; pore structure; fluid mobility

Citation: Hu, J.; Yang, S.; Jiang, Y.; Deng, H.; Wang, M.; You, L.; Li, Q.; Bai, H.; Shen, B. Experimental Study on Edge Water Invasion of Strongly Heterogeneous Carbonate Gas Reservoirs Based on NMR Technology. *Processes* **2024**, *12*, 1361. https://doi.org/10.3390/pr12071361

Academic Editor: Ottavia Giuffrè

Received: 10 June 2024
Revised: 25 June 2024
Accepted: 28 June 2024
Published: 29 June 2024

1. Introduction

Natural gas, a relatively clean energy source among conventional fossil fuels, has garnered increasing attention globally in the energy sector [1–5]. Carbonate gas reservoirs, which are widely distributed and possess enormous volumes, constitute a vital resource for oil and gas production worldwide [6,7]. Statistical data indicate that recoverable reserves of carbonate natural gas account for approximately 45% of the total recoverable natural gas reserves, with production contributing around 60% to the total natural gas output [8]. Notably, carbonate reservoirs exhibit diverse storage space types, are characterized by extensively developed cross-scale fractures, and display strong heterogeneity due to the interplay of multiple factors, including reservoir burial depth, high temperature, and high pressure. As a result, these reservoirs are marked by complex microscopic pore structures, which lead to intricate seepage laws.

Approximately 80% of carbonate gas reservoirs worldwide contain formation water bodies of varying sizes [9], and the primary recovery rate of edge/bottom water gas reservoirs typically does not exceed 50% [10]. Water invasion of gas reservoirs can lead to the formation of large-scale water-sealed gas in the reservoir, resulting in severe consequences, including reduced gas well productivity, premature closure of gas wells, and a significant decline in gas reservoir recovery rate. In reservoirs with developed fractures, formation water can rapidly channel along large-scale fractures, blocking numerous tiny throats and micro fractures on the fracture walls, thereby limiting gas supply in the main fractures and preventing gas production from matrix pores [11,12]. When water breakthrough occurs at the bottom of the well, the water saturation of the reservoir near the wellbore increases significantly, causing a decrease in the relative permeability of the gas phase, an increase in the gas abandonment pressure, and a decline in the gas reservoir recovery rate.

At present, the research on water invasion in gas reservoirs mainly focuses on the mechanism and evaluation of water invasion. The research methods mainly include physical experiments, numerical simulation, and mathematical formula calculation. Chen et al. [13] employed online NMR monitoring to investigate the water invasion mechanism and residual gas distribution in carbonate gas reservoirs, revealing that the residual gas distribution was influenced by the combined effects of fracture penetration, bottom water volume, fracture width, and gas well production. Guo et al. [14] combined molecular simulation with microscopic water injection experiments to study the distribution law of gas–water phases during water flooding, providing a quantitative evaluation of gas–water distribution in porous media. Zhang et al. [15] utilized NMR combined with centrifugation to examine the relationship between tight sandstone pore throat characteristics, fluid distribution, and gas reservoir water block mechanism, concluding that increased reservoir porosity and the formation of a complex fracture network facilitate more uniform water channeling along fractures during production, thereby slowing down the advancement of the water invasion front. Dong et al. [16] established a three-dimensional (3-D) coupled thermo-hydro-chemical model to investigate the drilling fluid invasion process and the dynamic response of natural gas hydrate reservoirs, finding that drilling fluid invasion characteristics primarily depend on drilling fluid pressure and permeability, while temperature affects hydrate dissociation. Yang et al. [17] developed an ideal fracture model using finite element technology to study the factors influencing water invasion depth, demonstrating that pressure difference and fracture width are negatively linearly related to water invasion depth, and that increased gas–water surface tension leads to deeper water invasion. Feng et al. [18] improved the quantitative description method of the matching relationship between pores, cavities, and fractures based on digital processing and analysis of full-diameter cores, analyzing the influence of various types of cavities and fractures on the water invasion law of reservoirs, and showing that fracture development exacerbates water invasion, while uniform cavity development slows it down. He et al. [19] employed microfluidic technology to investigate the underlying causes of water blocking damage in porous media and to identify suitable recovery methods. Their findings revealed that reducing the gas–liquid capillary pressure can effectively decrease the rate and quantity of spontaneous imbibition in cores. Moreover, water blocking damage can be mitigated to a certain extent by modifying the gas injection pressure, gas injection method, or adding wetting modifiers. While significant progress has been made in understanding the water invasion laws of various gas reservoirs, the research on water invasion patterns, water-locked gas formation mechanisms, and distribution characteristics of strongly heterogeneous carbonate reservoirs remains at a qualitative stage, lacking quantitative conclusions. Consequently, the existing knowledge is insufficient to support the development of efficient exploitation plans for these complex reservoirs.

As a non-destructive physical detection technology, NMR has been widely used in many fields such as materials science, medical imaging, and chemical analysis [20–22]. It is easy to see from the current research status that NMR technology has been widely used in the research field of water invasion in various gas reservoirs and has achieved good

results [15,23–25]. This paper takes the reservoir core of the fourth member of the Dengying Formation in the Penglai gas field, Sichuan Basin as the research object and conducts a systematic study on the pore throat structure, pore distribution, fluid mobility, dynamic gas production characteristics during water invasion, and the formation mechanism and distribution law of water-sealed gas in three types of strongly heterogeneous carbonate gas reservoirs. Initially, the pore types and development characteristics of carbonate gas reservoirs are thoroughly investigated through surface observation of natural cores, combined with cast thin sections and SEM images. Subsequently, the pore distribution law of different types of reservoirs and the fluid mobility of the reservoirs are studied by combining centrifugal technology with NMR testing. Finally, edge water invasion simulation experiments are conducted using natural cores under online NMR monitoring to investigate the formation mechanism and distribution law of water-sealed gas in various reservoirs. The research workflow is illustrated in Figure 1. The ultimate goal is to elucidate the impact of large-size pores, such as dissolved pores, cavities, and fractures, in carbonate reservoirs on microscopic water invasion behavior and their influence on gas reservoir recovery, thereby providing theoretical guidance for well layout and perforation development of such gas reservoirs.

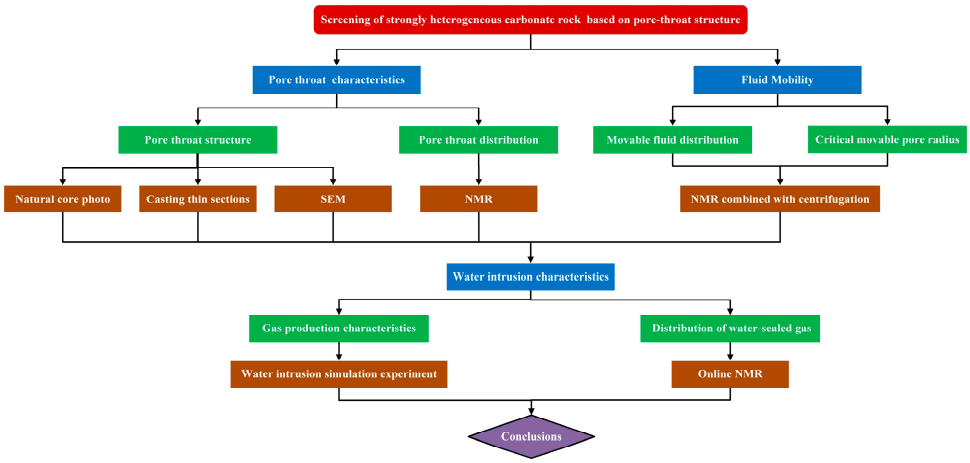

Figure 1. Schematic diagram of the research method and process.

2. Methodology

2.1. Material

The experimental core samples in this study were taken from the reservoir of the fourth member of the Dengying Formation in the Penglai Gas Field, Sichuan Basin. Based on porosity, permeability, pore-throat structure, and seepage characteristics, a total of 12 cores were rigorously classified into different reservoir types. Ultimately, one representative core from each of the three types of strongly heterogeneous carbonate rocks was selected. The detailed physical property parameters of the experimental cores, such as porosity, permeability, and well names are shown in Table 1. According to the formation water composition data in the study area, the $CaCl_2$ brine with a salinity of 52,172 mg/L was configured as the experimental simulation water. Additionally, nitrogen (without hydrogen) with a purity of 99.99 was used to simulate reservoir natural gas.

Table 1. Experimental parameters of core sample.

Sample Number	Length/cm	Diameter/cm	Permeability/10^{-3} μm^2	Porosity/%	Sample Type
1	4.424	2.501	0.695	4.431	Fracture type
2	4.135	2.497	0.431	5.863	Cavity type
3	4.235	2.499	1.732	7.221	Fracture-cavity type

2.2. Pore-Throat Structure Research Methods

2.2.1. Casting Thin Sections

The preparation process of cast thin sections strictly adhered the industry standard SY/T 5913-2004 of the People's Republic of China. The experimental environment was maintained at a constant temperature of 23 °C and relative humidity of 35%. Core samples were sectioned using a microtome and subsequently ground on a grinder workbench to a thickness of 0.1 mm. Further grinding with ultrafine diamond powder reduced the section thickness to 0.03 mm. The resulting cast thin sections were standardized to dimensions of 20 mm × 20 mm × 0.03 mm and impregnated with blue epoxy. Finally, the observation of lithological and pore throat space in the cast thin sections was conducted using a polarizing microscope (Axioskop 40, Zeiss, Oberkochen, Germany).

2.2.2. SEM

The preparation process of SEM thin sections strictly adhered the industry standard GB/T 18295-2001 of the People's Republic of China. The experimental environment was maintained at a constant temperature of 23 °C and relative humidity of 35%. All the SEM thin sections were cut to dimensions of 10 mm × 10 mm × 5 mm and subjected to a two-week washing procedure in a mixed organic solvent of benzene and methanol. Subsequently, the surfaces of SEM thin sections were polished and coated with a thin gold layer using an ion-sputtering apparatus (EM SCD500, Leica, Wetzlar, Germany). Finally, the observation of mineral components and pore throat space in the SEM thin sections was conducted using a scanning electron microscope (SU8010, Hitachi, Hitachi City, Japan).

2.3. NMR Methods

2.3.1. NMR Principles

NMR technology can measure the transverse relaxation time of formation pore fluids, thereby indirectly providing a number of key petrophysical parameters such as formation porosity, permeability, and fluid saturation [26,27]. The relationship of transverse relaxation time T_2 is mainly shown as follows:

$$\frac{1}{T_2} = \frac{1}{T_{2B}} + \frac{1}{T_{2S}} + \frac{1}{T_{2D}} \approx \frac{1}{T_{2S}} \quad (1)$$

where T_2 is the transverse relaxation time, ms; T_{2B} is the volume relaxation time, ms; T_{2S} is the surface relaxation time; and T_{2D} is the diffusion relaxation time, ms. Notably, the value of T_{2B} is significantly larger than that of T_{2S}, and its impact on T_2 is often negligible, thus it can be safely ignored. Furthermore, the influence of T_{2D} on T_2 is also negligible in a uniform static magnetic field. Moreover, T_{2s} can also be characterized by the following formula:

$$\frac{1}{T_{2S}} = \rho_s \frac{S}{V} = \rho_s \frac{F_S}{r_c} \quad (2)$$

where ρ_S is the transverse surface relaxation intensity, μm/ms; S/V is the specific surface area, 1/μm; F_s is the geometric shape factor, which takes a value of 2 for cylindrical pipes and 3 for spherical pores; and r_c is the radius of the pore throat, μm.

Combining Formulas (1) and (2), the relationship between T_2 and r_c can be obtained, as follows:

$$T_2 = \frac{r_c}{\rho_S F_S} = C \cdot r_c \quad (3)$$

Since ρ_S and F_s are constants, the reciprocal of their product can be represented by a constant C, implying a linear relationship between T_2 and r_c. It is well established that strongly heterogeneous carbonate reservoirs exhibit a diverse range of pore types and a considerable pore size span, encompassing nanometer to meter scales. In our previous study [28], distinct T_2 value intervals were employed to categorize pores of different sizes

in carbonate reservoirs, achieving good characterization results. In this study, we adopted the same approach to classify carbonate reservoir pore types based on their corresponding T_2 values, as shown in Figure 2.

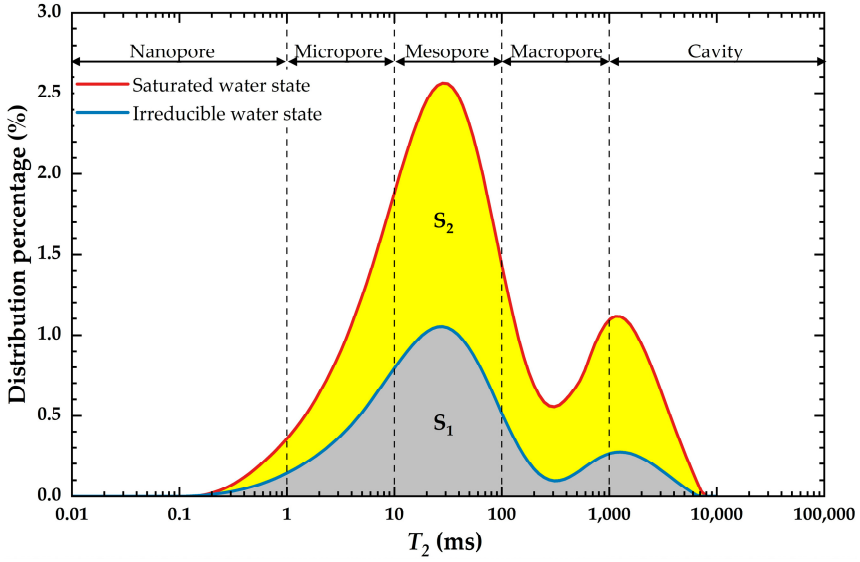

Figure 2. The T_2 range corresponding to different size of pores in carbonate reservoir. S_1 represents the pore size distribution of irreducible water; S_2 represents the pore size distribution of free fluid; and "S_1 + S_2" represents the pore size distribution of the core sample.

2.3.2. Characterization of Movable Fluid under Different Centrifugal Forces

First, the experimental core was evacuated and saturated with brine water until its mass remained constant. Subsequently, the fully saturated core was placed in NMR instrument (Geospec 2/53, Oxford, UK), and its T_2 spectrum line was measured in the saturated water state. The NMR instrument operated at a working frequency of 2 MHz with an error range of ±0.01 MHz, with 64 scans, an echo time of 0.27 ms, and a generated gradient magnetic field of 300 mT/m. It is worth noting that this type of instrument has yielded reliable testing results in numerous research studies [25,29,30]. Next, the experimental core was subjected to centrifugation using a high-speed centrifuge (H/T20MM, Herexi, Tianjin, China) at speeds of 1250, 2500, 3750, 6250, 12,500, and 37,500 n/min, respectively. Notably, the T_2 spectrum of the core was measured after each centrifugation step.

2.3.3. Characterization of Gas–Water Seepage Behavior during Edge Water Invasion

The online NMR monitoring system for the edge water intrusion simulation experiment consists of three primary components: a water body simulation subsystem, an NMR monitoring subsystem, and a gas–liquid two-phase metering subsystem (Figure 3). The core sample, centrifuged to the irreducible water state, is placed in a core holder (P5, Oxford, UK) with a maximum pressure and temperature capacity of 35 MPa and 80 °C, respectively. The confining pressure of the core holder is provided by a constant speed and pressure pump (HKV-N1, Haian, Ningbo, China), and the experimental confining pressure is maintained at 40 MPa. Subsequently, N_2 is continuously injected into the core sample using a high-pressure syringe pump (Teledyne Isco, Oillab, Burbank, CA, USA), causing the fluid pressure in the sample to rise to 30 MPa. Next, the core outlet pressure is controlled at 28 MPa using a constant speed and pressure pump, and synthetic brine is continuously injected into the core sample at a constant pressure of 30 MPa at the core inlet. During the brine injection process, real-time measurements of water and gas production at the core outlet are taken. When gas production at the core outlet ceases, the water injection operation is stopped, and the T_2 spectrum of the core is subsequently measured.

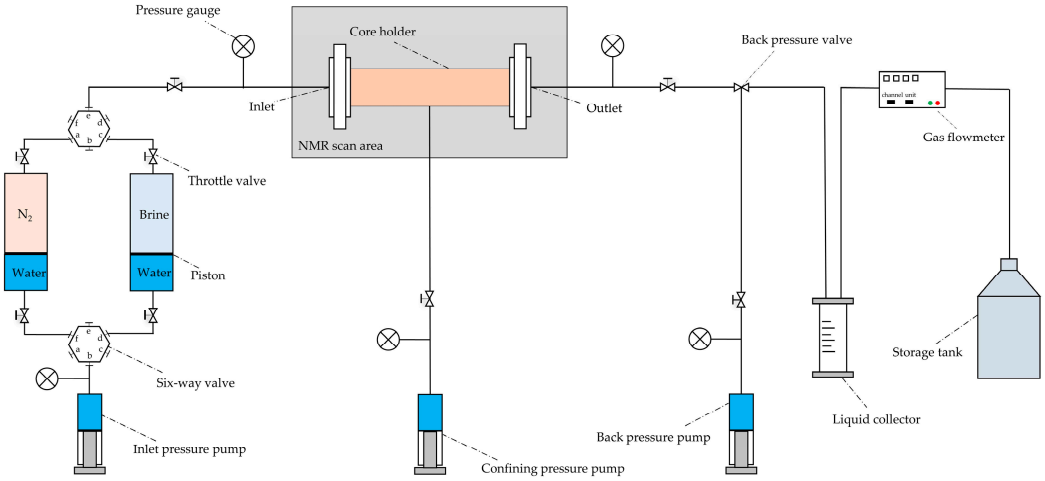

Figure 3. Flow chart of edge water invasion simulation experiment under online NMR monitoring.

3. Experimental Results and Discussion

3.1. Pore Throat Characteristics of Carbonate Reservoirs

3.1.1. Pore Throat Structural Characteristics

Based on the development characteristics of main pore types and macroscopic seepage laws of reservoirs, strongly heterogeneous carbonate gas reservoirs can typically be categorized into three types: fracture type, cavity type, and fracture–cavity type [31,32]. The photos of the reservoir plunger core from the fourth member of the Dengying Formation in the Penglai Gas Field (Figure 4a–c) reveal several high-angle stress fractures, low-angle dissolved fractures, and scattered dissolved pores on the surface of the fracture-type core. However, no cavities are observed on the surface of the fracture-type core, and most pores are too small to be observed with the naked eye. This suggests that the fracture-type core has weak storage capacity but strong seepage capacity. In contrast, the cavity-type core exhibits cavities and dissolved pores of varying sizes on its surface, but most cavities are isolated and distributed. Furthermore, only one fracture filled with minerals, thereby lacking seepage capability, is observed on the surface of the cavity-type core. This indicates that the cavity-type core has strong storage capacity but weak seepage capacity. The fracture–cavity core, however, displays a diverse range of pore types on its surface, including cavities, fractures, and dissolved pores, with a close spatial relationship between cavities and fractures. The cavity–fracture network system facilitates both gas storage and gas seepage, making fracture–cavity reservoirs the highest-quality carbonate reservoir type [33,34].

Figure 4d–f presents cast thin section images of three types of strongly heterogeneous carbonate reservoir cores. Several large-sized fractures developed inside the fracture-type core, interconnecting to form an irregular fracture network that divides the entire rock sample into matrix areas of different sizes. Additionally, several micro fractures are scattered throughout the matrix area, which can significantly improve local seepage capacity [35]. The seepage capacity of fracture-type core is controlled by the fracture network, resulting in strong spatial heterogeneity. In contrast, the cavities within the cavity-type core exhibit an obviously isolated distribution, with no fractures or thick throats between cavities for diversion. Typically, medium- and large-sized cavities are connected by multiple throats from different directions, featuring good connectivity, whereas small-sized cavities have only a few or even lack connected throats with poor connectivity. The fracture–cavity core, however, features various types of throats, including tubular throats and necking throats, and fractures of different sizes, which have greatly enhanced pore connectivity, making this type of core possess a fracture–cavity pore network with both strong storage capacity and seepage capacity.

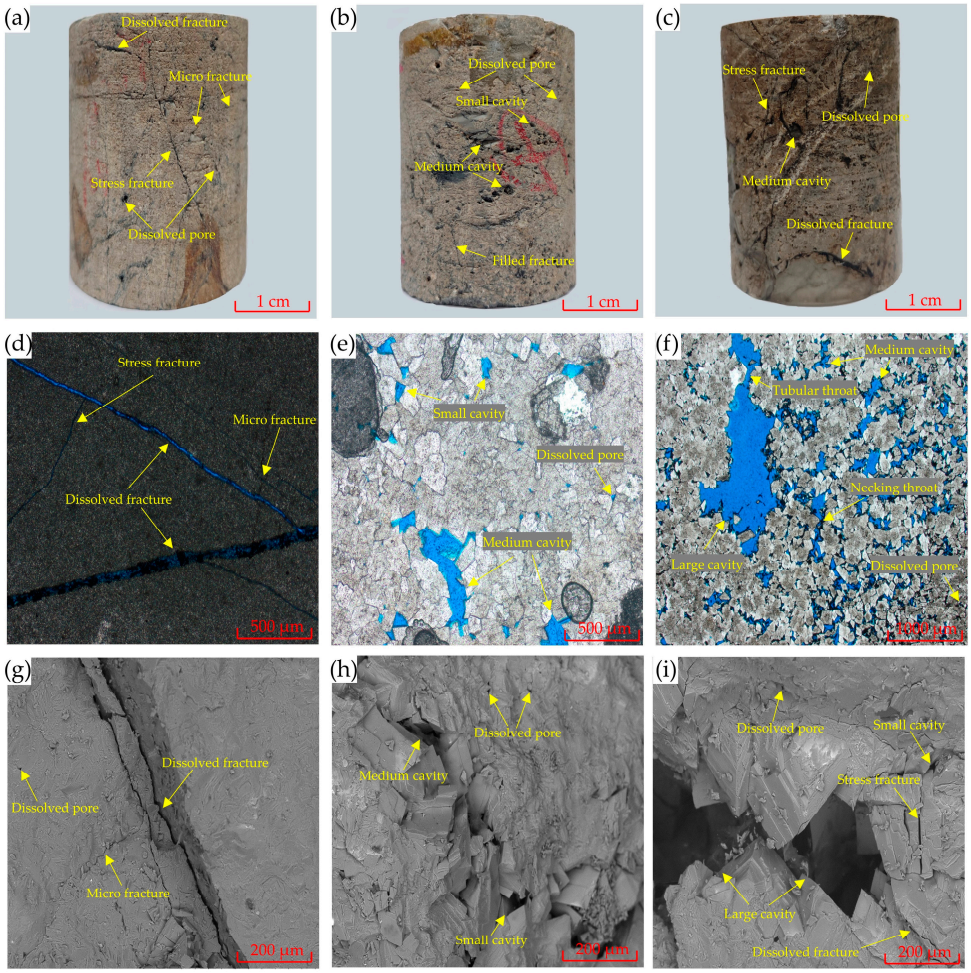

Figure 4. Photos, Casting thin sections and SEM images of three typical types of carbonate cores: (**a**) PS-6 well, 6975.62–6975.70 m, fracture type, dissolved fracture, stress fracture and micro fracture developed; (**b**) PS-9 well, 6980.50–6980.67 m, cavity type, cavity, dissolved pore and filled fracture developed; (**c**) PS-11 well, 6986.66–6986.83, fracture–cavity type, cavity, fracture and dissolved pore developed; (**d**) fracture type, stress fracture, dissolved fracture and micro fracture developed; (**e**) cavity type, cavity and dissolved pore developed; (**f**) fracture–cavity type, cavity, necking and tubular throats developed; (**g**) fracture type, dissolved pore, dissolved fracture and micro fracture developed; (**h**) cavity type, dissolved pore and cavity developed; (**i**) fracture–cavity type, cavity, fracture and dissolved pore developed.

Figure 4g–i displays SEM images of three types of strongly heterogeneous carbonate reservoir cores. Studies have shown that the permeability of natural fractures generally surpasses that of matrix pores by several orders of magnitude in the Sichuan Basin [36]. In the fracture-type core, although high-permeability fractures constitute a small fraction of the pore space, they significantly enhance the heterogeneity of this core. Consequently, in fractured edge or bottom-water gas reservoirs, formation water can easily channel along the fracture pathways, leading to premature water breakthrough at the bottom of the gas well and a subsequent decline in productivity [37]. In the cavity-type core, cavities occupy a large part of the pore space and are the most important pore type. The presence of cavities can significantly improve the local seepage capacity of rocks; however, because the cavities are isolated from each other, they cannot form a dominant seepage channel throughout the entire rock sample. In the fracture–cavity core, the development of a fracture–cavity pore network allows a large amount of gas in the cavities to be quickly recovered. This is the most fundamental reason for the long-term high and stable production of gas wells in fracture–cavity reservoirs [38].

3.1.2. Pore Throat Distribution Characteristics

Figure 5a shows the T_2 spectral lines of three types of strongly heterogeneous carbonate cores in the water-saturated state. Notably, the T_2 spectral lines of three core samples exhibit completely distinct distribution characteristics. The T_2 spectral line of Sample 1 (fracture-type) exhibits a single peak, with a corresponding T_2 value of 74.82 ms. The entire T_2 spectral line of it is distributed within the range of 0.10 ms to 382.54 ms, indicating that the internal pores of the fracture-type core are predominantly small-sized, with few macropores and essentially no cavities. In contrast, the T_2 spectral line of Sample 2 (cavity type) features a bimodal distribution, with T_2 values of 28.11 ms and 1135.32 ms corresponding to the left and right peak positions, respectively. This suggests that two sets of pores, one coarse and one fine, are developed within the cavity-type core, but mainly fine pores. The T_2 spectral line of Sample 3 (fracture–cavity type) is characterized by a broad peak, with the T_2 valve concentrated between 34.94 ms and 1018.30 ms. This indicates that the fracture–cavity core contains a variety of pores, with mesopores and macropores being the primary ones.

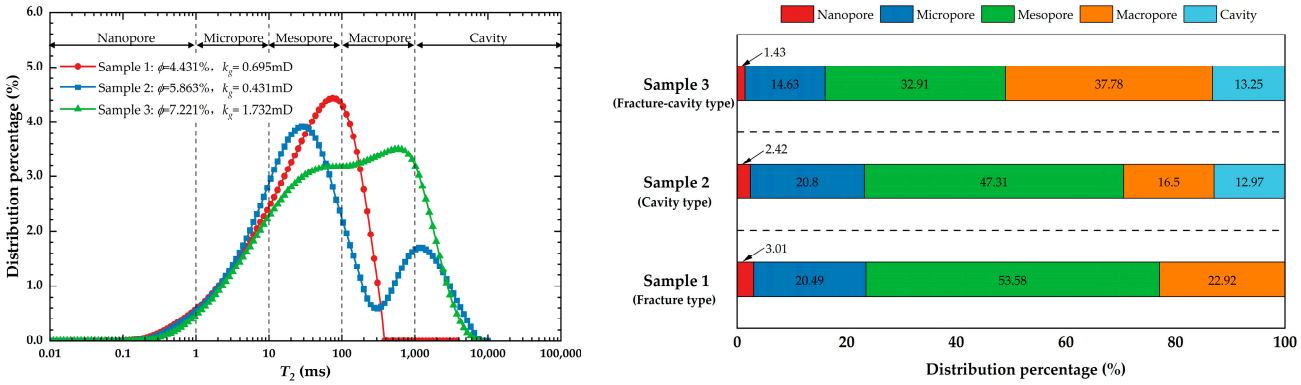

(**a**) (**b**)

Figure 5. Pore distribution characteristics based on NMR: (**a**) T_2 spectrum line under the saturated water state and (**b**) pore type percentage. φ = porosity; k_g = gas permeability measured with nitrogen.

Figure 5b displays the percentage distribution of different pore types in three types of strongly heterogeneous carbonate rock samples, classified according to the standards outlined in Section 2.3.1. Notably, mesopores are the dominant pore type in both Sample 1 and Sample 2, accounting for 53.58% and 47.31%, respectively. In contrast, macropores are the most abundant pore type in Sample 3, comprising 37.78%. Compared to Sample 1, Samples 2 and 3 exhibit a higher proportion of cavities, which are crucial for enhancing local seepage capacity, accounting for 13.25% and 12.97%, respectively. Nanopores are the pore type with the smallest proportion and contribute the least to the gas storage capacity of carbonate gas reservoirs, accounting for only 3.01%, 2.42%, and 1.43%, respectively, in the three samples. The distinct percentage distributions of different pore types in the three types of strongly heterogeneous carbonate gas reservoirs reflect the varying types and intensities of diagenetic transformations that occurred during their geological history, resulting in unique seepage laws for each reservoir type.

3.2. Movable Fluid Distribution

3.2.1. Movable Fluid Distribution under Different Centrifugal States

Movable fluid saturation, referring to the saturation corresponding to fluid with actual mobility in rock pores, is a crucial parameter that comprehensively reflects the interaction between reservoir fluid and pore throat surface, fluid physical properties, pore throat structure, and pore connectivity [29]. Figure 6 displays the T_2 spectrum distribution curve under different centrifugal speeds of the three types of strongly heterogeneous carbonate rock samples. As the centrifugation rate increases, the area enveloped by the T_2 spectral line of the core sample gradually decreases, indicating a gradual increase in the movable fluid

saturation of the core sample. However, when the centrifugation rate reaches 37,500 n/min, the shape and area of the T_2 spectral line of the core sample remain almost unchanged, and the water-containing state of the core at this time is considered to be the irreducible water state. Notably, the hydrogen core signal intensity corresponding to different T_2 values does not decrease simultaneously, reflecting the microscopic heterogeneity of pore connectivity. Interestingly, for Sample 1, the decrease in hydrogen core signal intensity corresponding to mesopores is significantly higher than that of macropores, suggesting that, compared to pore size, the size and number of connected throats are the key to determining the mobility of the pore fluid [39].

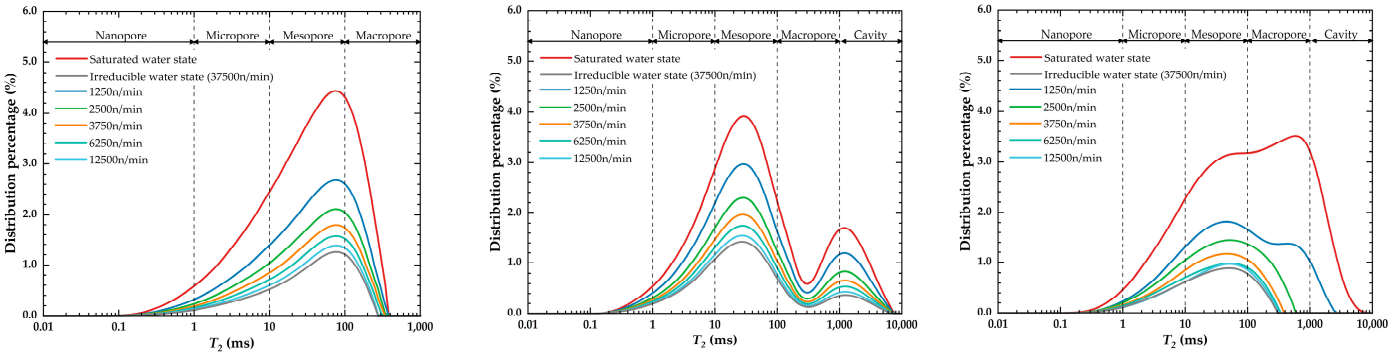

Figure 6. T_2 spectrum distribution curve under different centrifugal speeds: (**a**) Sample 1, fracture-type; (**b**) Sample 2, cavity-type and (**c**) Sample 3, fracture–cavity type.

Figure 7 shows the movable fluid saturation under different centrifugal speeds of the three types of strongly heterogeneous carbonate rock samples. The movable fluid saturation of the core sample increases rapidly with the increase in centrifugal speed, but the growth rate decreases quickly. At low centrifugal speeds, the fluid in a large pore-coarse throat only needs to overcome a small flow resistance to flow. In contrast, the centrifugal force applied to the fluid in a small pore-thin throat is insufficient to overcome the large flow resistance, rendering it temporarily immobile. As the centrifugal speed continues to increase, more and more fluids in small pore throats gradually become mobile. However, when the centrifugal speed reaches 37,500 n/min (a very large value), a certain amount of immobile water still exists in some pore spaces. At this point, the movable fluid saturation of the core reaches its maximum. The maximum movable fluid saturations of Sample 1, Sample 2, and Sample 3 are 76.63%, 67.77%, and 84.05%, respectively. This indicates that fracture–cavity samples exhibit the strongest fluid mobility, while cavity-type samples exhibit the weakest. Furthermore, compared to cavities, fractures can enhance the mobility of fluid in rock pores more significantly. For instance, when the centrifugal speed reaches 1250 n/min, the movable fluid saturation of Sample 1 reaches 38.15%, whereas that of Sample 2 is only 25.75%.

Table 2 presents a detailed distribution of water-bearing pores in three types of carbonate rock samples under saturated water and irreducible water states. Compared to the saturated water state, the proportions of various types of water-bearing pores in the core samples under the irreducible water state decreased to varying degrees. The more significant the decrease in the proportion of a certain type of water-bearing pores in the core sample, the better the pore throat structure of this type of pore and the stronger the fluid mobility. The proportion of water-bearing cavities in Sample 3 under the saturated water state is 13.25%, which rapidly drops to 0 after only a centrifugal operation at a speed of 2500 n/min (Figure 6c). This indicates that the cavities in the fracture-cavity reservoir exhibit super strong fluid mobility, with a maximum movable fluid saturation of 100%. This is also the fundamental reason why fracture–cavity reservoirs firmly occupy the main gas production position in various carbonate reservoirs. In contrast, due to the lack of fracture

development, the fluid mobility of the cavities in the cavity-type reservoirs is much weaker. Under the irreducible water state, the proportion of water-bearing cavities in Sample 2 is still notable (2.56%). Additionally, except for cavities in Samples 1 and 3, other pore types in the three samples have a certain proportion under the irreducible water state. This suggests that the size of fluid mobility in rock pores is controlled by multiple factors, including pore structure, pore throat size, and pore connectivity [40].

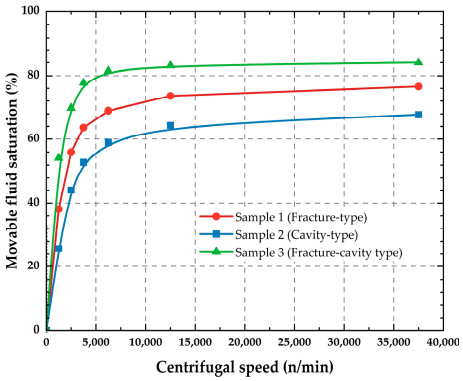

Figure 7. Movable fluid saturation under different centrifugal speeds.

Table 2. Distribution of water-bearing pores under saturated water state and irreducible water state.

Sample Number	Hydrated State	Nanopore (%)	Micropore (%)	Mesopore (%)	Macropore (%)	Cavity (%)
1	Saturated water state	3.01	20.49	53.58	22.92	0
	Irreducible water state	0.57	4.24	13.67	4.85	0
2	Saturated water state	2.42	20.8	47.31	16.5	12.97
	Irreducible water state	0.88	7.78	17.15	3.95	2.56
3	Saturated water state	1.43	14.63	32.91	37.78	13.25
	Irreducible water state	0.35	3.95	9.14	2.59	0

3.2.2. Critical Movable Pore Radius

The T_2 cutoff value, which represents the T_2 dividing value between bound fluid and movable fluid in the T_2 spectrum, is a crucial parameter that reflects the mobility of reservoir fluid [41]. In contrast to the T_2 cutoff value obtained by empirical statistical methods, the data obtained by combining NMR testing with centrifugation experiments on reservoir cores are more accurate and reliable [42]. According to the principle of T_2 cutoff value, the smaller the T_2 cutoff value of the reservoir, the smaller the critical movable pore radius and the greater the fluid mobility of the reservoir. Figure 8 shows the T_2 spectrum and corresponding T_2 cutoff values of three types of strongly heterogeneous carbonate core samples in the water-saturated state and the bound water state. The T_2 value corresponding to the data point on the T_2 cumulative distribution curve in the saturated water state that is equal to the maximum cumulative percentage of T_2 in the irreducible water state is the T_2 cutoff value.

The T_2 cutoff values of Sample 1, Sample 2, and Sample 3 are 9.47 ms, 15.48 ms, and 8.98 ms, respectively. It is clear that the T_2 cutoff values of Sample 1 and Sample 3, which both exhibit developed fractures, are relatively close, whereas there is a significant difference between them and the T_2 cutoff value of Sample 2, which only has cavities but lacks fractures. This indicates that the existence of fractures can significantly reduce the critical movable pore radius, thereby improving the fluid mobility of the reservoir, while this effect of caves is relatively weak. It is noteworthy that the T_2 cutoff value method is an idealized approach that reflects the overall fluid mobility of the reservoir and has certain limitations. This method assumes that the fluid in pores with throat sizes below the T_2 cutoff value is completely immobile, which is not entirely consistent with the actual reservoir situation. As revealed by the experimental data and analysis in Section 3.2.1, pore throat size is not the only factor that determines the fluid mobility of the reservoir. In fact,

the fluid in the nanopores (<1 ms) of the core samples from the three types of carbonate gas reservoirs all exhibits a certain degree of mobility (Figure 6a–c).

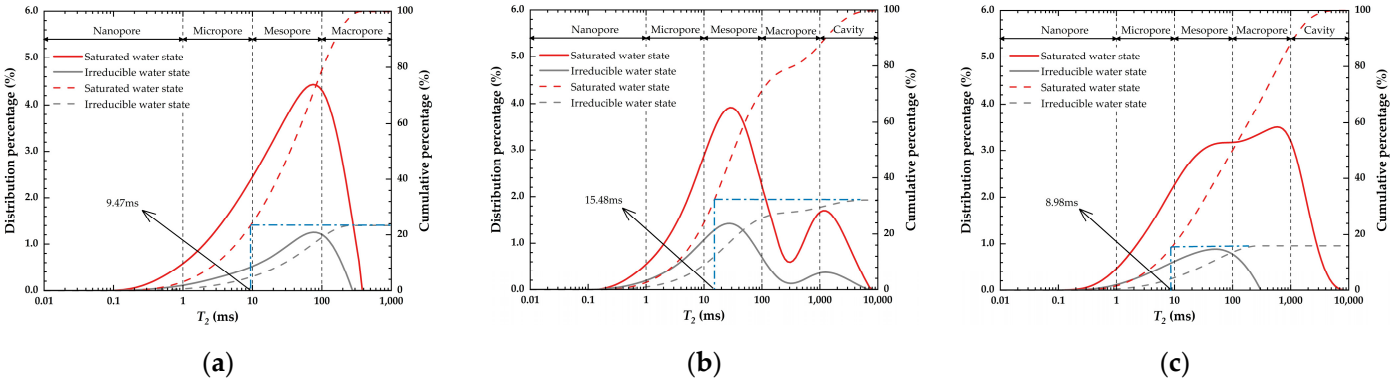

Figure 8. T_2 spectrum distribution curve in saturated water state and irreducible water state, along with the corresponding T_2 cutoff value: (**a**) Sample 1, fracture-type; (**b**) Sample 2, cavity-type and (**c**) Sample 3, fracture–cavity type.

3.3. Water Invasion in Edge Water Gas Reservoirs

3.3.1. Reservoir Dynamic Gas Production Characteristics

Identifying gas reservoir water invasion types and conducting real-time monitoring of gas–water ratios in gas wells are crucial tasks in the dynamic analysis of gas reservoir development with edge or bottom water [10]. Water invasion simulation experiments enable accurate simulation of the dynamic process of gas reservoir water invasion, thereby facilitating effective predictions of production performance and recovery rates for gas reservoirs with edge or bottom water [43]. Figure 9 illustrates the temporal variation of gas production rate, water-gas ratio and gas recovery rate for the three types of cores in the water invasion simulation experiment. Meanwhile, Table 3 further presents key parameters reflecting the gas production characteristics of the core samples in the water invasion simulation experiment. The gas production period of the core can be categorized into two distinct stages based on whether water is produced at the core outlet: pure gas production and gas–water co-production. It is apparent that different types of cores exhibit unique gas production patterns and water–gas ratio variation patterns during these two stages.

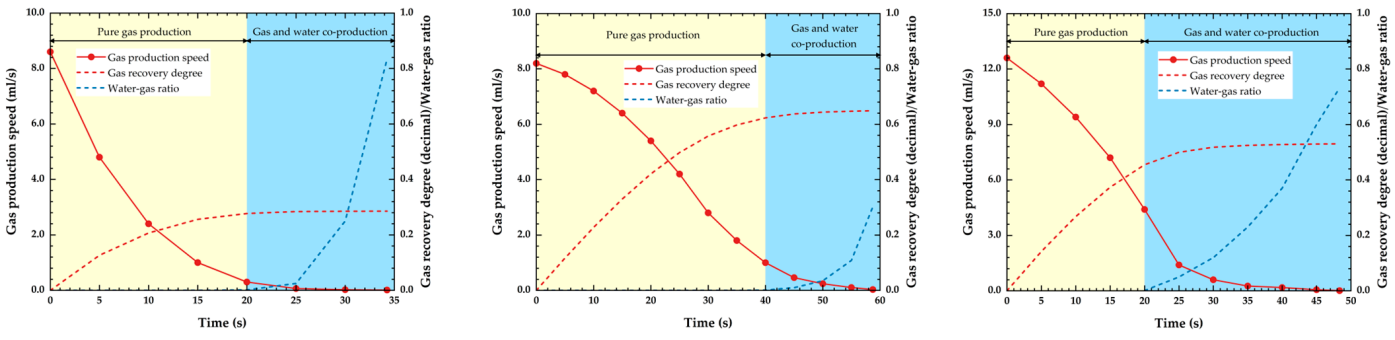

Figure 9. Gas production characteristics of core samples during edge water invasion: (**a**) Sample 1, fracture-type; (**b**) Sample 2, cavity-type and (**c**) Sample 3, fracture–cavity type.

During the initial pure gas production stage, Sample 1 exhibited high gas production capacity, which was attributed to the rapid flow of gas through the fractures. However, the matrix pores in Sample 1 were constrained by their relatively low permeability, limiting their ability to supply gas to the fractures, resulting in a rapid decline in the gas production

rate of the core. At approximately 20 s, water production commenced at the core outlet, followed by a rapid increase in the water–gas ratio. The premature water breakthrough at the core outlet caused severe water lock and water seal, resulting in a large amount of gas being trapped by water and difficult to produce [44]. The gas recovery factors for Sample 1 during the pure gas production stage and the gas–water co-production stage were 29.11% and 0.70%, respectively. This indicates that the majority of recoverable gas in fracture-type cores is produced during the pure gas production stage, and gas recovery after water breakthrough at the core outlet is significantly limited.

Table 3. Key parameters of gas production in core samples during edge water invasion.

Sample Number	Production Time (s)	Ultimate Water-Gas Ratio	Gas Recovery Degree (%)		
			Pure Gas Stage	Gas and Water Stage	Total
1	34.26	0.83	29.11	0.70	29.81
2	58.74	0.65	62.30	2.57	64.87
3	48.35	0.72	45.49	7.54	53.03

The pure gas production stage of Sample 2 lasted for up to 40 s, the longest among the three core types. During this stage, the gas production rate of Sample 2 decreased more slowly than that of Sample 1, which can be attributed to the relatively uniform advancement of synthetic brine inside the cavity-type core. This uniform advancement is supported by the slowly rising water–gas ratio, enabling the timely recovery of a large amount of gas in the cavities. As a result, the ultimate gas recovery rate of Sample 2 reached as high as 64.87%, the highest among the three core types. Similar to Sample 1, most of the recoverable gas in the cavity-type core was produced during the pure gas production stage, with only 2.57% of the gas recovered after water breakthrough at the core outlet.

During the pure gas production stage, Sample 3 exhibited an initial gas production rate of up to 12.6 mL/s, but this was accompanied by a rapid decline. Similar to Sample 1, Sample 3 began to produce water after 20 s of pure gas production. However, in contrast to Sample 1, Sample 3 maintained a high gas production rate while producing water. Ultimately, the gas recovery rate of Sample 3 during the gas–water co-production period reached 7.54%, significantly higher than the 0.70% gas recovery rate of Sample 1 during the same period. This phenomenon can be attributed to the fact that, after water breakthrough at the outlet of the fracture-type core, its internal fractures are largely filled with water, thereby hindering the flow of gas from the small-sized matrix pores into the fractures. In contrast, non-uniform water invasion inside the fracture–cavity core allows the unrecovered gas in some cavities to still flow into the fractures, even after water breakthrough at the core outlet.

The ultimate gas recovery rates of Samples 1, 2, and 3 were 29.81%, 64.87%, and 53.03%, respectively. Notably, Sample 1 was most severely impacted by water invasion, whereas Sample 2 was least affected. This suggests that the presence of fractures exacerbates reservoir water invasion, while the presence of cavities mitigates the adverse effects of water invasion. However, analyzing the variation of core gas production and gas–water ratio only provides a relatively macroscopic understanding of the water invasion gas production law in the three types of carbonate gas reservoirs. To further elucidate the microscopic water invasion mechanism and water-sealed gas distribution characteristics in the cross-scale pores of heterogeneous carbonate gas reservoirs, it is essential to employ online NMR technology to monitor water invasion behavior in the core pore space. This will be discussed in detail in the next section.

3.3.2. Formation Mechanism and Distribution Characteristics of Water-Sealed Gas

Figure 10 shows the T_2 spectra line of invasion water and closed gas in three types of strongly heterogeneous carbonate reservoir cores after water invasion. Table 4 further

summarizes the proportion of invasion water and closed gas in various types of pores. The T_2 spectra lines corresponding to the invasion water and closed gas of Sample 1 both exhibit a single peak, indicating a relatively uniform distribution of closed gas in various pores within the fracture-type core. Notably, the cumulative proportion of invasion water in various pore spaces of Sample 1 is only 22.47%, whereas the cumulative proportion of closed gas is as high as 54.05%. Furthermore, the proportion of closed gas in medium and large pores in Sample 1 is the largest, totaling 41.4%. This strongly suggests that fractures are the primary cause of the pronounced heterogeneous water invasion phenomenon in fractured reservoirs. Even when a small amount of formation water flows rapidly along the fractures, a significant amount of gas in the matrix pores becomes trapped and cannot be produced.

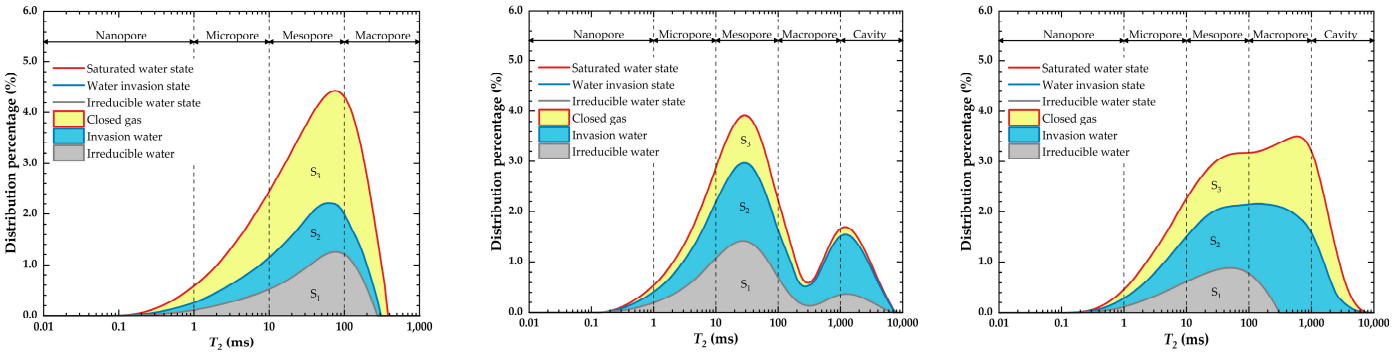

Figure 10. Distribution curve of closed gas and invasion water in core samples after water invasion: (**a**) Sample 1, fracture-type; (**b**) Sample 2, cavity-type and (**c**) Sample 3, fracture–cavity type. S_1 represents the T_2 distribution of irreducible water; S_2 represents the T_2 distribution of invasion water; S_3 represents the T_2 distribution of closed gas.

Table 4. The proportion of invasion water and closed gas in various pores.

Sample Number	Fluid Type	Nanopore (%)	Micropore (%)	Mesopore (%)	Macropore (%)	Cavity (%)
1	Invasion water	0.77	5.23	12.83	3.64	0
	Closed gas	1.66	10.99	27.00	14.40	0
2	Invasion water	0.96	8.16	18.88	9.49	9.08
	Closed gas	0.59	5.00	11.59	2.94	1.15
3	Invasion water	0.53	5.55	13.09	20.41	5.42
	Closed gas	0.55	5.15	10.73	14.79	7.82

The T_2 spectrum line of the invasion water in Sample 2 exhibits a bimodal distribution, whereas the T_2 spectrum line of the closed gas is characterized by a single peak with a relatively fine skewness. The proportion of closed gas in various pore spaces in Sample 2 totals 21.27%, primarily distributed in small-sized pores, with only 4.09% in macropores and cavities. This indicates that, in contrast to fracture-type reservoirs, the water invasion process in cavity-type reservoirs is significantly more uniform, allowing for the majority of the gas in cavities and macropores to be produced, while only some gas in matrix pores is sealed by invasion water. The primary reason for this difference lies in the distinct functional roles of cavities and fractures due to their morphological differences. Natural fractures, with long extensions and small openings, possess strong conductivity but weak storage capacity. This fundamental characteristic is responsible for the rapid decline in production rate during the pure gas production stage in fracture-type cores. In contrast, cavities, with large diameters and limited extensions, exhibit strong storage capacity but weak conductivity. The robust storage capacity of cavities enables them to store more invasion water, thereby slowing the advancement of the water invasion front. This is also the primary reason for the long pure gas production period in cavity-type core.

In Section 3.2.1, we revealed that the fracture–cavity pore network serves as the primary seepage channel in fracture–cavity reservoirs, and the cavity is the only pore type with a movable fluid saturation of up to 100%. However, surprisingly, the proportion of closed gas in the cavity of Sample 3 reaches 7.82%, even higher than that in the cavity of Sample 2. These two phenomena are not inherently contradictory. Since most reservoir rocks exhibit water-wet wettability (relative to gas) and the mobility between formation water and natural gas is relatively high, the mobility of formation water in pores is primarily influenced by the rock's pore structure during NMR tests combined with centrifugation. In contrast, during water invasion experiments, the mobility of gas in pores is affected not only by the rock's pore structure but also by the distribution of formation water. The presence of formation water in pore throats reduces the flow space of the gas phase and increases its flow resistance. In extreme cases, the gas in the pore loses its ability to flow due to complete water blockage of the throat, resulting in water-sealed gas. The development of fractures within fracture–cavity reservoirs indicates an extremely uneven water invasion process. Although the presence of cavities can slow down the advancement of the water invasion front to some extent, the uneven advancement of formation water along multiple fractures cannot be completely avoided, which is also the main reason for the early water breakthrough in fracture–cavity cores.

4. Discussion

The gas–water relationship in carbonate gas reservoirs is typically more complex. Considering various geological factors, such as formation dip, water body scale, and interlayer distribution in the reservoir, the water invasion phenomenon in actual reservoirs is far more complicated than the situation involved in core simulation water invasion experiments. In constructing the physical model, this study neglected these geological factors and potential chemical reactions between formation water, natural gas, and carbonate rock. Instead, it focused on investigating the pore-throat structure, particularly the specific effects of cavities and fractures on water invasion behavior. In reality, natural gas in gas reservoirs is impure and contains impurities such as CO_2, N_2, and H_2S. During long-term water invasion, chemical reactions inevitably occur between formation water and carbonate rocks, leading to the dissolution of rock minerals and the generation of new minerals, which alter the porosity and permeability of the reservoir and even pose the risk of caprock leakage. Furthermore, the research on the water invasion behavior of large-scale pores in carbonate gas reservoirs in this study is still at the stage of qualitative understanding. In the future, numerical simulation software can be employed to quantitatively study how large-size pores affect the formation of water-locked gas and its impact on natural gas recovery.

5. Conclusions

This study integrates natural core photographs, cast thin sections, and scanning electron microscope images to qualitatively characterize the pore throat structure characteristics of three types of strongly heterogeneous reservoirs in carbonate gas reservoirs. Furthermore, NMR tests were employed to quantitatively characterize the pore distribution characteristics of these three types of reservoirs, based on the division of T_2 values for different types of pores. Additionally, the fluid mobility of different types of pores in the three types of reservoirs was investigated by combining NMR tests with centrifugal experiments. Finally, the water invasion simulation experiments were conducted under online NMR monitoring, and the dynamic gas production law of the cores of the three types of reservoirs during water invasion, as well as the formation mechanism and distribution law of closed gas after water invasion, were analyzed and discussed. The conclusions are as follows:

(1) The T_2 spectrum of the fracture-type reservoir in the saturated water state displays a single peak, indicative of a reservoir with small overall pore size and limited storage capacity. However, its well-developed irregular fracture network confers strong seepage capacity. In contrast, the T_2 spectrum of the cavity-type reservoir exhibits a bimodal distribution, featuring two distinct sets of pore throat systems, one coarse

and one fine, developed internally. Despite its strong storage capacity, the lack of fractures for fluid diversion restricts its seepage capacity. The fracture–cavity network system in the fracture–cavity reservoir endows it with excellent storage capacity and seepage capacity, but also introduces strong heterogeneity to this type of reservoir.

(2) The maximum movable fluid saturations of the three types of reservoirs, namely fracture-type, cavity-type, and fracture–cavity reservoirs, are 76.63%, 67.77%, and 84.05%, respectively, with corresponding T_2 cut-off values of 9.47 ms, 15.48 ms, and 8.98 ms, respectively. These data indicate that the fracture–cavity type reservoir exhibits the strongest fluid mobility, whereas the cavity-type reservoir displays the weakest fluid mobility. This can be attributed to the fact that fractures can significantly enhance the connectivity of reservoir pores, thereby improving the fluid mobility of the reservoir, whereas the effect of cavities on pore connectivity is relatively weak.

(3) The water invasion simulation experiment revealed that the ultimate recovery rates of fracture-type reservoirs, cavity-type reservoirs, and fracture–cavity reservoirs were 29.81%, 64.87%, and 53.03%, respectively. Notably, fracture-type reservoirs were most susceptible to water invasion, whereas cavity-type reservoirs were least affected. The formation water flows along and through the fractures in the reservoir, resulting in premature water breakthrough at the well bottom, which consequently seals a significant amount of gas in the matrix pores, rendering it unrecoverable. In contrast, the cavities in the reservoir possess a strong storage capacity, enabling them to effectively retard the advancement of the water invasion front, thereby alleviating the adverse impact of water invasion.

Author Contributions: Conceptualization, S.Y.; methodology, S.Y.; validation, H.D.; formal analysis, M.W.; investigation, H.B.; resources, Q.L.; data curation, J.H.; writing—original draft preparation, J.H.; writing—review and editing, B.S.; visualization, J.H.; supervision, S.Y.; project administration, L.Y.; funding acquisition, Y.J. All authors have read and agreed to the published version of the manuscript.

Funding: This research was funded by the Sichuan Provincial Natural Science Foundation Project, grant number 2023NSFSC0261.

Data Availability Statement: The data presented in this study are available through email upon request to the corresponding author.

Conflicts of Interest: Authors Yi Jiang, Hui Deng, Mengyu Wang were employed by the company PetroChina Southwest Oil & Gasfield Company. Author Hui Deng was employed by the company Sichuan Petroleum Administration Co., Ltd. The remaining authors declare that the research was conducted in the absence of any commercial or financial relationships that could be construed as a potential conflict of interest.

References

1. Ding, J.; Yan, C.; Wang, G.; He, Y.; Zhao, R. Competitive Adsorption between CO_2 and CH_4 in Tight Sandstone and Its Influence on CO_2-Injection Enhanced Gas Recovery (EGR). *Int. J. Greenh. Gas Control* **2022**, *113*, 103530. [CrossRef]
2. Gao, X.; Yang, S.; Tian, L.; Shen, B.; Bi, L.; Zhang, Y.; Wang, M.; Rui, Z. System and Multi-Physics Coupling Model of Liquid-CO_2 Injection on CO_2 Storage with Enhanced Gas Recovery (CSEGR) Framework. *Energy* **2024**, *294*, 130951. [CrossRef]
3. Zhao, E.; Jin, Z.; Li, G.; Zhang, K.; Zeng, Y. Numerical Simulation of CO_2 Storage with Enhanced Gas Recovery in Depleted Tight Sandstone Gas Reservoirs. *Fuel* **2024**, *371*, 131948. [CrossRef]
4. Li, Q.; Liu, J.; Wang, S.; Guo, Y.; Han, X.; Li, Q.; Cheng, Y.; Dong, Z.; Li, X.; Zhang, X. Numerical Insights into Factors Affecting Collapse Behavior of Horizontal Wellbore in Clayey Silt Hydrate-Bearing Sediments and the Accompanying Control Strategy. *Ocean Eng.* **2024**, *297*, 117029. [CrossRef]
5. Hu, J.; Yang, S.; Yang, K.; Deng, H.; Wang, M.; Li, J.; Gao, X. Enhanced Gas Recovery Coupled with CO_2 Sequestration in Tight Sandstone Reservoirs with Different Pore-Throat Structures. *Energy Fuels* **2024**. [CrossRef]
6. Xu, Z.; Li, S.; Li, B.; Chen, D.; Liu, Z.; Li, Z. A Review of Development Methods and EOR Technologies for Carbonate Reservoirs. *Pet. Sci.* **2020**, *17*, 990–1013. [CrossRef]
7. Li, Q.; Wang, Y.; Wang, F.; Wu, J.; Tahir, M.U.; Li, Q.; Yuan, L.; Liu, Z. Effect of Thickener and Reservoir Parameters on the Filtration Property of CO_2 Fracturing Fluid. *Energy Sources Part A-Recovery Util. Environ. Eff.* **2020**, *42*, 1705–1715. [CrossRef]
8. Ma, X.; Yan, H.; Chen, J.; He, D.; Xu, W. Development Patterns and Constraints of Superimposed Karst Reservoirs in Sinian Dengying Formation, Anyue Gas Field, Sichuan Basin. *Oil Gas Geol.* **2021**, *42*, 1281–1294. [CrossRef]

9. Huang, S.; Liu, J.; Sun, J.; Geng, M. Water Invasion Mode of Carbonate Gas Reservoirs Controlled by Edge Water: Three Invasion Modes. *Front. Energy Res.* **2022**, *10*, 860527. [CrossRef]
10. Hu, Y.; Chen, Y.; Li, T. The formation development and theoretical connotations of Review of the effect of temperature on oil-water relative permeability "overall water control of gas reservoir" technology in gas field development. *Nat. Gas Ind.* **2022**, *42*, 10–20. [CrossRef]
11. Zhang, R.; Lu, G.; Peng, X.; Li, L.; Hu, Y.; Zhao, Y.; Zhang, L. Study on the Mechanism of Gas-Water Two-Phase Flow in Carbonate Reservoirs at Pore Scale. *Petroleum* **2023**, S2405656123000664. [CrossRef]
12. Liu, Y.; Tong, T.A.; Ozbayoglu, E.; Yu, M.; Upchurch, E. An Improved Drift-Flux Correlation for Gas-Liquid Two-Phase Flow in Horizontal and Vertical Upward Inclined Wells. *J. Pet. Sci. Eng.* **2020**, *195*, 107881. [CrossRef]
13. Chen, P.; Liu, H.; Zhao, H.; Guo, C.; Xing, Y.; Cheng, M.; Shi, H.; Zhang, L.; Li, Y.; Su, P. Microscopic Characteristics of Water Invasion and Residual Gas Distribution in Carbonate Gas Reservoirs. *Energy Sci. Eng.* **2021**, *9*, 2151–2164. [CrossRef]
14. Guo, P.; Zhou, R.; Tian, Z.; Wang, Y.; Yan, L.; Zhao, J.; Yu, C. Gas and Water Distribution Characteristics of Water-Driven Gas Process in Tight Sandstone Gas Reservoirs: A Microscale Study by Molecular Simulation and Experiment. *Energy Rep.* **2022**, *8*, 7025–7036. [CrossRef]
15. Zhang, J.; Tang, Y.; Wang, H.; Huang, L.; Liao, F.; Liu, Y.; Chen, Y. Study on the Mechanism of Water Blocking in Tight Sandstone Gas Reservoirs Based on Centrifugal and Nuclear Magnetic Resonance Methods. *Energies* **2022**, *15*, 6680. [CrossRef]
16. Dong, L.; Wan, Y.; Li, Y.; Liao, H.; Liu, C.; Wu, N.; Leonenko, Y. 3D Numerical Simulation on Drilling Fluid Invasion into Natural Gas Hydrate Reservoirs. *Energy* **2022**, *241*, 122932. [CrossRef]
17. Yang, J.; Li, C.; Geng, S.; He, S.; Li, K. Microscopic Flow Mechanism of Water Invasion in Ideal Fracture Models. *Energy Sources Part A-Recovery Util. Environ. Eff.* **2020**, 1–13. [CrossRef]
18. Feng, X.; Peng, X.; Li, L.; Yang, X.; Wang, J.; Li, Q.; Zhang, C.; Deng, H. Influence of Reservoir Heterogeneity on Water Invasion Differentiation in Carbonate Gas Reservoirs. *Nat. Gas Ind. B* **2019**, *6*, 7–15. [CrossRef]
19. He, F.; Wang, J. Study on the Causes of Water Blocking Damage and Its Solutions in Gas Reservoirs with Microfluidic Technology. *Energies* **2022**, *15*, 2684. [CrossRef]
20. Fowler, N.J.; Williamson, M.P. The Accuracy of Protein Structures in Solution Determined by AlphaFold and NMR. *Structure* **2022**, *30*, 925–933. [CrossRef]
21. Aslam, N.; Pfender, M.; Neumann, P.; Reuter, R.; Zappe, A.; de Oliveira, F.F.; Denisenko, A.; Sumiya, H.; Onoda, S.; Isoya, J.; et al. Nanoscale Nuclear Magnetic Resonance with Chemical Resolution. *Science* **2017**, *357*, 67–71. [CrossRef] [PubMed]
22. Jin, Y.; Kneusels, N.-J.H.; Marbella, L.E.; Castillo-Martinez, E.; Magusin, P.C.M.M.; Weatherup, R.S.; Jonsson, E.; Liu, T.; Paul, S.; Grey, C.P. Understanding Fluoroethylene Carbonate and Vinylene Carbonate Based Electrolytes for Si Anodes in Lithium Ion Batteries with NMR Spectroscopy. *J. Am. Chem. Soc.* **2018**, *140*, 9854–9867. [CrossRef] [PubMed]
23. Wang, R.; Zhang, C.; Chen, D.; Yang, F.; Li, H.; Li, M. Microscopic Seepage Mechanism of Gas and Water in Ultra-Deep Fractured Sandstone Gas Reservoirs of Low Porosity: A Case Study of Keshen Gas Field in Kuqa Depression of Tarim Basin, China. *Front. Earth Sci.* **2022**, *10*, 893701. [CrossRef]
24. Zhou, M.; Li, X.; Hu, Y.; Xu, X.; Jiang, L.; Li, Y. Physical Simulation Experimental Technology and Mechanism of Water Invasion in Fractured-Porous Gas Reservoir: A Review. *Energies* **2021**, *14*, 3918. [CrossRef]
25. Liao, G.-Z.; Chen, W.-L.; Zong, F.-R.; Deng, F.; Liu, H.-B.; Wu, B.-S.; Liu, W.; Sun, Z.; Luo, S.-H. NMR Fluid Analyzer Applying to Petroleum Industry. *Pet. Sci.* **2021**, *18*, 54–91. [CrossRef]
26. Zhao, Y.; Sun, Y.; Liu, S.; Wang, K.; Jiang, Y. Pore Structure Characterization of Coal by NMR Cryoporometry. *Fuel* **2017**, *190*, 359–369. [CrossRef]
27. Liu, Z.; Liu, D.; Cai, Y.; Yao, Y.; Pan, Z.; Zhou, Y. Application of Nuclear Magnetic Resonance (NMR) in Coalbed Methane and Shale Reservoirs: A Review. *Int. J. Coal Geol.* **2020**, *218*, 103–261. [CrossRef]
28. Hu, J.; Yang, S.; Wang, B.; Deng, H.; Wang, M.; Li, J.; Zhao, S.; Shen, B.; Gao, X.; Yang, K. Effect of Pore Structure Characteristics on Gas-Water Seepage Behaviour in Deep Carbonate Gas Reservoirs. *Geoenergy Sci. Eng.* **2024**, *238*, 212–881. [CrossRef]
29. Liu, G.; Xie, S.; Tian, W.; Wang, J.; Li, S.; Wang, Y.; Yang, D. Effect of Pore-Throat Structure on Gas-Water Seepage Behaviour in a Tight Sandstone Gas Reservoir. *Fuel* **2022**, *310*, 121–901. [CrossRef]
30. Xu, R.; Yang, S.; Li, M.; Wang, J.; Dong, Z.; Xie, P.; Jin, Y.; Wang, X. Experimental Study on Unstable Imbibition Characteristics of Fracturing Fluids at High Pressures and Temperatures in the Tight Continental Reservoir. *Geoenergy Sci. Eng.* **2023**, *221*, 211–362. [CrossRef]
31. Zou, C.; Du, J.; Xu, C.; Wang, Z.; Zhang, B.; Wei, G.; Wang, T.; Yao, G.; Deng, S.; Liu, J.; et al. Formation, Distribution, Resource Potential, and Discovery of Sinian–Cambrian Giant Gas Field, Sichuan Basin, SW China. *Pet. Explor. Dev.* **2014**, *41*, 306–325. [CrossRef]
32. Hu, J.; Yang, S.; Wang, B.; Yan, Y.; Deng, H. Trinomial Capacity Equation for Horizontal Wells in Deep Carbonate Gas Reservoirs: Case Study of Dengying Formation in Anyue Gas Field, Sichuan Basin. *Nat. Gas Geosci.* **2023**, *34*, 1112–1122.
33. Wang, L.; Yang, S.; Liu, Y.; Xu, W.; Deng, H.; Meng, Z.; Han, W.; Qian, K. Experiments on Gas Supply Capability of Commingled Production in a Fracture-Cavity Carbonate Gas Reservoir. *Pet. Explor. Dev.* **2017**, *44*, 824–833. [CrossRef]
34. Liu, Y.; Upchurch, E.R.; Ozbayoglu, E.M. Experimental Study of Single Taylor Bubble Rising in Stagnant and Downward Flowing Non-Newtonian Fluids in Inclined Pipes. *Energies* **2021**, *14*, 578. [CrossRef]

35. Zhang, D.; Zhang, L.; Guo, J.; Zhou, Y.; Zhao, Y. Research on the Production Performance of Multistage Fractured Horizontal Well in Shale Gas Reservoir. *J. Nat. Gas Sci. Eng.* **2015**, *26*, 279–289. [CrossRef]
36. Zeng, L.; Gong, L.; Guan, C.; Zhang, B.; Wang, Q.; Zeng, Q.; Lyu, W. Natural Fractures and Their Contribution to Tight Gas Conglomerate Reservoirs: A Case Study in the Northwestern Sichuan Basin, China. *J. Pet. Sci. Eng.* **2022**, *210*, 110028. [CrossRef]
37. Fang, F.; Shen, W.; Li, X.; Gao, S.; Liu, H.; Li, J. Experimental Study on Water Invasion Mechanism of Fractured Carbonate Gas Reservoirs in Longwangmiao Formation, Moxi Block, Sichuan Basin. *Environ. Earth Sci.* **2019**, *78*, 316. [CrossRef]
38. Haijun, Y.; Dongbo, H.; Ailin, J.; Zhiping, L.; Jianlin, G.; Xian, P.; Fankun, M.; Xinyu, L.; Zhanmei, Z.; Hui, D.; et al. Characteristics and Development Model of Karst Reservoirs in the Fourth Member of Sinian Dengying Formation in Central Sichuan Basin, SW China. *Pet. Explor. Dev.* **2022**, *49*, 810–823. [CrossRef]
39. Qin, Y.; Yao, S.; Xiao, H.; Cao, J.; Hu, W.; Sun, L.; Tao, K.; Liu, X. Pore Structure and Connectivity of Tight Sandstone Reservoirs in Petroleum Basins: A Review and Application of New Methodologies to the Late Triassic Ordos Basin, China. *Mar. Pet. Geol.* **2021**, *129*, 105084. [CrossRef]
40. Ouyang, S.; Lu, X.; Zhang, Y.; Chen, L.; Qu, Y.; Sun, W. Impacts of the Pore-Throat Structure on Fluid Mobility in Tight Sandstone: Insight from an Improved Method Based on Rate-Controlled Porosimetry and Nuclear Magnetic Resonance. *Energy Fuels* **2023**, *37*, 273–290. [CrossRef]
41. Xiao, L.; Li, J.; Mao, Z.; Lu, J.; Yu, H.; Guo, H.; Li, G. A Method to Determine Nuclear Magnetic Resonance (NMR) T_2 Cutoff Based on Normal Distribution Simulation in Tight Sandstone Reservoirs. *Fuel* **2018**, *225*, 472–482. [CrossRef]
42. Wu, S.; Li, S.; Yuan, X.; Yang, Z.; Li, A.; Cui, J.; Pan, S.; Mao, Z.; Su, L.; Zhou, Y. Fluid Mobility Evaluation of Tight Sandstones in Chang 7 Member of Yanchang Formation, Ordos Basin. *J. Earth Sci.* **2021**, *32*, 850–862. [CrossRef]
43. Shusheng, G.; Minghan, Y.; Liyou, Y.; Huaxun, L.; Wenqing, Z. Simulation experiment of water invasion performance in low-permeability bottom water gas reservoir and its influence on recovery factor. *Nat. Gas Ind.* **2022**, *42*, 61–70. [CrossRef]
44. Liu, D.; Yao, Y.; Yuan, X.; Yang, Y. Experimental Evaluation of the Dynamic Water-Blocking Effect in Coalbed Methane Reservoir. *J. Pet. Sci. Eng.* **2022**, *217*, 110887. [CrossRef]